This manuscript has been submitted to EarthArXiv as a non-peer-reviewed preprint and is intended for subsequent submission to a remote sensing–focused journal.

A Low-Cost In-Silico Geological Assessment Workflow for Two IOCG-Style Targets with Mixed Iron-Oxide Surface Expression in Chile, with Comparative Reference to a Copper Porphyry Gossan-Blanket System

Horst Kutsch[1], Kentaro Takasaki[2]

[1]*Katholische Universität Eichstätt-Ingolstadt, Faculty of Mathematics and Geography, Germany
[2]Sophia University, Graduate School of Global Environmental Studies (GENV), Tokyo, Japan

* Corresponding author: horst.kutsch@ku.de

Abstract

This study presents a low-cost, in-silico geological assessment workflow for early-stage mineral exploration under minimal-data conditions, with particular relevance for artisanal mining and small-scale exploration. Contrasting Chilean case settings are used to examine differences in oxidized surface expression. The analysis focuses on two targets in the Chilean Coastal Cordillera cobalt–iron belt, where mixed iron oxide signatures form heterogeneous, structurally controlled surface patterns consistent with an IOCG-style setting, and compares them with a laterally coherent gossan-blanket surface in the Precordillera of central Chile. Geological interpretation was derived exclusively from remotely sensed data, combining very-high-resolution RGB imagery from Airbus Pléiades with RGB–HSV transformation, object-based image analysis, and morphometric evaluation of slope and erosional texture. Particular emphasis is placed on datasets based only on RGB imagery, where enhanced spatial detail can partly compensate for the absence of diagnostic hyperspectral bands used in prospect-scale targeting. The workflow reconstructs geological meaning entirely from digital image interpretation, without field calibration or analytical input. Results show that this approach can support coherent prospect-scale reasoning under minimal-data conditions, while requiring subsequent validation through mapping, trenching, drilling, and analytical confirmation. The study highlights the potential and limitations of accessible, image-based exploration workflows for artisanal mining and low-resource exploration contexts.

Keywords

IOCG, hydrothermal alteration, iron oxide surface expression, mineral exploration, remote sensing, satellite imagery, Google Earth, object-based image analysis, geomorphometry, low-cost exploration, Chile

Introduction

Remote sensing has become an established component of early-stage mineral exploration, particularly in settings where surface alteration patterns, structural controls, and geomorphological contrasts can be evaluated prior to field deployment (JICA, 2005, Chapter 5, Section 5.1.1). In many published studies, such approaches are implemented within comparatively sophisticated analytical environments, including hyperspectral imagery, multispectral band-ratio analysis, derived statistical transformations, and integrated geospatial modeling (Badr et al., 2026; El-Wardany et al., 2025; Mohamed et al., 2023; Orynbassarova et al., 2025; van der Meer et al., 2012).

By contrast, fewer studies have examined how far geological interpretation can be extended under minimal-data conditions, where analysis relies exclusively on low-cost or freely accessible imagery without field calibration, laboratory mineralogy, or geochemical support. While not focused on geological surface patterning, Hu et al. (2013) demonstrated that Google Earth imagery can support object-based land-surface interpretation, indirectly suggesting its broader applicability in arid-region surface assessment. Although Google Earth imagery has been employed in geological studies for lineament mapping and terrain visualization (Lawal et al., 2022), and high-resolution Google Earth (GE/GE Pro) views have occasionally served as ancillary aids for feature discrimination within Landsat- or ASTER-based hydrothermal alteration workflows rather than as primary sources for alteration mapping (Fotze et al., 2019; Mahanta & Maiti, 2021), it has rarely been treated as a principal interpretive source for alteration-pattern assessment in mineral exploration.

The present study contributes to this domain not by claiming conceptual novelty, but by testing the interpretive value and transferability of a low-cost, fully digital workflow in a Chilean geological setting characterized by contrasting tectonic controls and surface-expression regimes. The approach was developed for two target prospects in the Chilean Coastal Cordillera cobalt–iron belt and is implemented entirely through remotely sensed data and digital inference. Geological interpretation was derived from a combination of freely accessible and commercial satellite imagery, principally Airbus Pléiades scenes acquired on 22 August and 7 September 2023 and accessed via Google Earth (2026), complemented by Sentinel-2 imagery provided by the European Space Agency (ESA) for comparative purposes. RGB values were converted to HSV following the classical transformation logic described by Smith (1978), with later implementation refinements documented by Chernov et al. (2015). This transformation was applied in combination with object-based image analysis (OBIA), morphometric evaluation of slope and erosional texture, and heuristic proxy mapping of iron oxide–related surface expressions (Blaschke, 2010; Arabameri et al., 2020; Pour & Hashim, 2012).

The workflow was designed to identify alteration zonation, oxidation fronts, morphostructural controls, and iron oxide–related surface contrasts in a target environment where mineralization is not expressed as a laterally coherent gossan blanket, but rather as a heterogeneous and

structurally mediated assemblage of surface signatures. This complexity is further compounded by the fact that Cu–Au mineralization is not consistently associated with iron oxide–rich breccias or with intense K-feldspar- or sericite-rich K–Fe alteration typical of many IOCG deposits worldwide (Blein et al., 2025).

In the principal study area in the Chilean Coastal Cordillera, the method was used to distinguish among patchy hematite-dominant surfaces, goethite-limonite-bearing zones, possible magnetite-related domains, and texturally variable pale or “frosted” terrains, while also resolving structurally guided drainage and erosional patterns that may locally imitate alteration textures. The interpretive challenge in this setting lies in the ambiguity of the surface expression: iron oxide distribution is discontinuous, lithologically and structurally influenced, and less readily diagnosable by direct visual inspection than in more classical gossan-dominated systems. Particular emphasis was therefore placed on the value of very-high-resolution RGB-only datasets, in which enhanced spatial detail can partially compensate for the absence of diagnostic hyperspectral bands typically used in prospect-scale targeting and early drill-site planning (Hajaj et al., 2024).

Within this context, the paper proposes the term *in-silico geological assessment* for a class of exploration workflows in which geological meaning is reconstructed entirely within a digital inference environment from remote-sensing proxies and physically grounded image interpretation. The concept is not presented as a substitute for hyperspectral surveys, field geology, mineralogical analysis, or geochemical verification, but rather as a zero- to very-low-budget pre-exploration methodology for rapid target screening, structural interpretation, and prioritization of subsequent field campaigns. The present case study therefore illustrates both the potential and the limitations of such an approach: it can support coherent prospect-scale geological reasoning from minimal observational inputs, but it does not replace the need for subsequent validation through mapping, trenching, drilling, and analytical confirmation (Upadhyay, 2025). Its practical significance lies primarily in early-stage screening and target prioritization rather than in definitive resource confirmation.

Beyond its methodological implications, this accessibility also extends the relevance of the approach to low-resource exploration settings, including small-scale and artisanal mining. Operators in such contexts often lack access to advanced remote-sensing datasets, specialized software environments, or the training required to interpret abstract analytical procedures such as principal component analysis or spectral band-ratio schemes. In contrast, the visual assessment of iron oxide color distributions and related surface contrasts provides a more intuitive basis for preliminary geological reasoning, closely aligned with observational practices already used in field prospecting.

Because Google Earth imagery is widely accessible, easy to disseminate, and straightforward to interpret visually, it may serve as a practical low-cost tool for early-stage alteration-pattern assessment in settings where technical capacity and financial resources are limited. This

interpretation is also consistent with Chilean institutional initiatives encouraging the adoption of modern AI and digital technologies in support of small-scale mining operations (Advanced Mining Technology Center [AMTC], 2021).

Materials and Methods

Study Area

The two study sites (Target 1 and Target 2) are located in the Coastal Cordillera of northern Chile (Atacama Region), more than 80 km west of the Pan-American Highway and the Atacama Fault. The Coastal Cordillera constitutes a 1,000–2,000 m high Mesozoic arc basement shaped by Jurassic–Early Cretaceous extensional tectonics, major sinistral strike-slip structures such as the Atacama Fault System (AFS), and subsequent Late Cretaceous–Cenozoic compressional deformation (González et al., 2003; Scheuber & González, 1999).

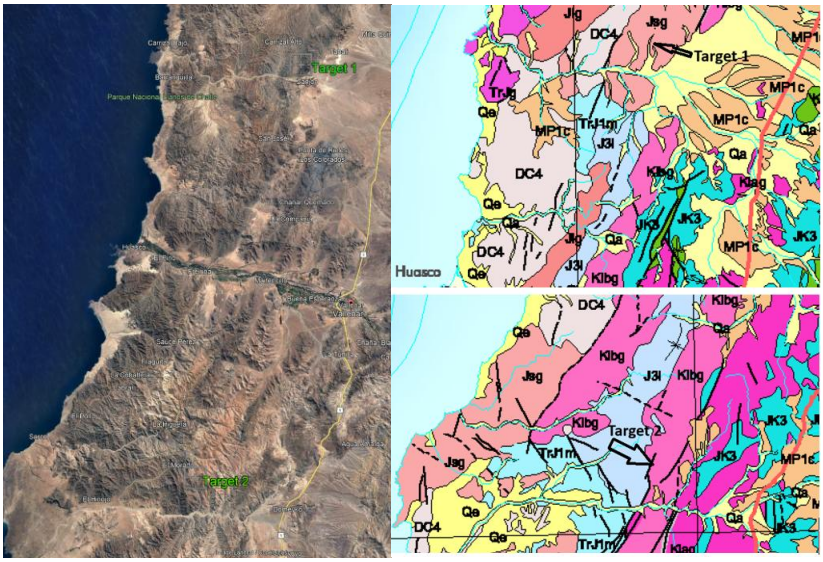

Figure 1. Regional setting and geological context of the study area in the Coastal Cordillera, Atacama Region, northern Chile. Left: Airbus Pléiades satellite imagery acquired in 2023 and visualised/annotated in Google Earth in 2026, showing the locations of Target 1 (WGS84: 28.126503° S, 70.863286° W) and Target 2 (WGS84: 28.894861° S, 71.089119° W) within the coastal–inland morphostructural framework west of the Pan-American Highway. Base imagery: Google Earth/Google Earth Pro; Pléiades imagery © CNES/Airbus DS where indicated. Annotations by the authors. Upper right: extract of the regional geological map showing the lithostratigraphic framework and structural elements surrounding Target 1. Lower right: corresponding geological map extract for Target 2. Geological information is derived from the available digital map display of *Mapa Geológico de Chile: Versión Digital* (SERNAGEOMIN, 2003; Publicación Geológica Digital No. 4; scale 1:1,000,000). The geological-map legend and translated unit descriptions are provided in Supplementary Figure S1.

An area associated with Upper Miocene granitoids in the Central Andean metallogenic belt of Chile was selected for comparative analysis. The granitoid, interpreted as potentially fertile, occurs within a broader assemblage of Middle- to Late Miocene plutonic complexes commonly regarded as barren (Deckart et al., 2010). Despite having been mapped by Chilean geologists, the intrusion remains unexplored to date.

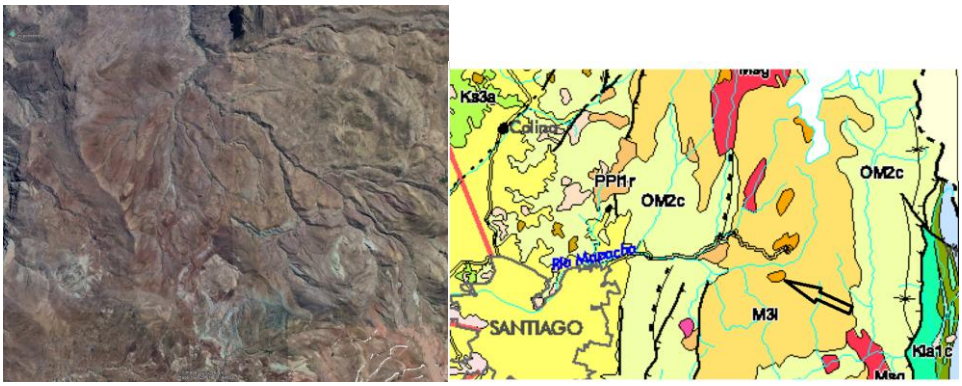

Figure 2. Reference example from the Central Andes of Chile illustrating surface expression above an Upper Miocene granitoid within the Andean metallogenic belt. Left: Airbus Pléiades satellite imagery acquired on 19 March 2024 and visualized and annotated in Google Earth in 2025, showing a red-dominated surface pattern developed over a granitoid intrusion. Base imagery: Google Earth/Google Earth Pro; Pléiades imagery © CNES/Airbus DS where indicated. Right: geological information derived from the available digital map display of *Mapa Geológico de Chile: Versión Digital* (SERNAGEOMIN, 2003; Publicación Geológica Digital No. 4; scale 1:1,000,000). The geological-map legend and translated unit descriptions are provided in Supplementary Figure S2.

Data Sources

Geological interpretation was based exclusively on remotely sensed data, comprising high-resolution optical satellite imagery and regional geological map information. Airbus Pléiades imagery (2023–2024 acquisitions) was accessed and visualized via Google Earth Pro (2025–2026), providing very-high-resolution data suitable for detailed surface-textural analysis. Published Pléiades specifications indicate a native spatial resolution of approximately 0.70 m, with standard visual products typically resampled to 0.50 m.

For regional comparison and spectral context, Sentinel-2 multispectral imagery (European Space Agency) was additionally consulted. In contrast to Pléiades data, Sentinel-2 true-color imagery provides visible bands at a spatial resolution of 10 m.

Geological framework information was derived from the digital geological map of Chile (Servicio Nacional de Geología y Minería [SERNAGEOMIN], 2003), at a scale of 1:1,000,000, providing lithostratigraphic classification and regional structural context.

All datasets were used without field calibration, geochemical validation, or systematic ground-truth control, consistent with the study's in-silico, minimal-data approach.

Although no formal field calibration or systematic validation was undertaken, contextual field-related evidence is indirectly reflected in the satellite imagery. At both Target 1 and Target 2, small-scale artisanal excavation features are visible, and at Target 2, indications of rudimentary ore processing activity can be identified. These features provide qualitative support for the presence of mineralized material, but were not used for calibration or quantitative validation of the remote sensing interpretation.

Image Processing and Analytical Workflow

RGB imagery was converted to HSV color space on a pixel-by-pixel basis using the standard transformation. This representation was adopted because it separates hue, saturation, and brightness, which proved more suitable than raw RGB values for the interpretive discrimination of surface color domains relevant to oxidized alteration mapping. Full computational details are provided in the Supplementary Material. The conversion follows the classical formulation of Smith (1978), in which value (V), saturation (S), and hue (H) are defined as follows: $V = \max(R,G,B)$, $S = [V - \min(R,G,B)]/V$ for $V \neq 0$, and H is defined piecewise depending on the dominant RGB component. Prior to transformation, RGB values were normalized to the [0,1] range. While alternative implementations exist (e.g., integer-based formulations; Chernov et al., 2015), these do not affect the interpretive use of HSV components in the present workflow.

Following transformation, HSV components were mapped back to the image domain on a pixel-wise basis, preserving the spatial resolution of the source imagery. Each pixel was represented by a triplet (H, S, V), enabling the generation of raster layers corresponding to individual HSV components. These layers were evaluated both independently and in combination to enhance discrimination of iron oxide–related surface expressions. In particular, hue variations were used to distinguish subtle color differences associated with hematite- versus goethite-dominated surfaces, saturation served as a proxy for color purity, and value retained information on brightness and topographic shading. This pixel-wise representation allowed spatial patterns of alteration-related color variation to be interpreted within their geomorphological and structural context.

The computational analysis was performed on raster imagery derived from Google Earth Pro. The analyzed subset for Target 1 (Figure 4) comprises approximately $1.2–1.4 \times 10^6$ pixels at the nominal visual resolution of Pléiades imagery (~0.5 m), corresponding to an areal extent of about 0.3 km². The analysis window for Target 2 (Figure 11) is estimated to comprise approximately $1.0–3.2 \times 10^6$ pixels at the same nominal resolution, based on its spatial extent. RGB values within these domains were transformed and evaluated iteratively across HSV component layers.

Although RGB-to-HSV transformation is a standard procedure, the workflow required repeated treatment of large raster populations at scene scale. In this context, AI-assisted tools were used

to structure the workflow, support coding, and refine text, thereby contributing to the efficient handling, internal consistency, and reproducibility of the image-based assessment.

To move beyond purely pixel-based color interpretation, the HSV-derived raster layers were further analyzed using object-based image analysis (OBIA), morphometric evaluation, and heuristic proxy mapping. Image segmentation was applied to group pixels into spatially coherent objects based on spectral similarity and local variance in HSV space, thereby reducing pixel-level noise and enabling analysis of geomorphologically meaningful units. Segmentation was guided by thresholds in hue and saturation contrast as well as textural homogeneity, approximating region-growing or clustering approaches commonly used in OBIA workflows. In practice, clustering of pixel populations was implemented using a Mini-Batch KMeans algorithm (as implemented in the scikit-learn Python library), allowing efficient segmentation of large datasets within HSV color space.

Morphometric evaluation was subsequently conducted by analyzing slope gradients, drainage patterns, and surface roughness inferred from shading and erosional textures visible in the imagery. This involved qualitative–quantitative assessment of brightness gradients (V component), directional texture patterns, and valley–ridge relationships, enabling differentiation between lithologically controlled color variation and topographically induced illumination effects.

Heuristic proxy mapping was implemented as a rule-based classification scheme in which combinations of HSV properties, visual texture, and spatial context were assigned to interpretive surface classes (Table S1). The approach builds on the separation of hue, saturation, and value/brightness in the HSV color model (Smith, 1978), and is consistent with remote-sensing applications in which HSV transformations have been used to organize spectral, lithological, and topographic information into geologically interpretable image products (Kurata & Yamaguchi, 2019). In the present study, the HSV-based framework is used as a conservative image-interpretation aid rather than as a mineralogically verified classification scheme. The rules therefore do not constitute strict spectral classification in a hyperspectral sense, but instead define physically informed proxies linking color-space behavior to mineralogical and geomorphological surface expressions.

The resulting framework represents a semi-quantitative decision tool in which spectral response, spatial coherence, visual texture, and geomorphological context are jointly evaluated. The rule set was iteratively refined through visual cross-comparison of HSV-derived layers, OBIA segmentation results, and spatial patterns to ensure internal consistency across the interpreted scene. Integration of these layers with morphometric context produced a composite false-color interpretation in which distinct tonal domains correspond to provisional alteration-related surface conditions, including oxidized gossan zones, hydrothermal alteration halos, clay-rich slope deposits, weakly altered host rock, and localized moisture-related features. The resulting

map supports delineation of structurally controlled mineralization pathways and prioritization of exploration targets. The overall analytical workflow is summarized schematically in Figure 3.

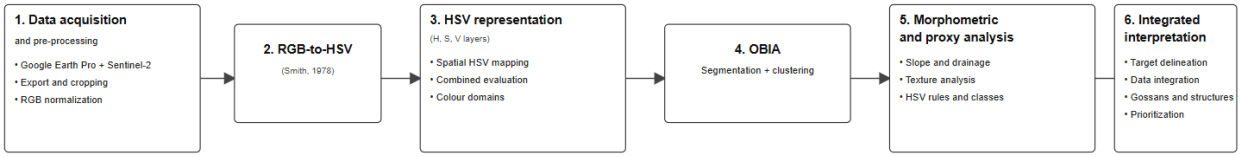

Figure 3. Schematic overview of the image-processing and analytical workflow applied in this study, presented in a left-to-right (landscape) sequence. The workflow comprises (1) data acquisition and pre-processing of very-high-resolution Airbus Pléiades imagery and Sentinel-2 data, including normalization and cropping to target polygons; (2) RGB-to-HSV transformation; (3) pixel-wise representation and evaluation of hue, saturation, and value (HSV) raster layers; (4) object-based image analysis (OBIA) through segmentation and clustering of spatially coherent units; (5) morphometric evaluation and heuristic proxy mapping based on HSV characteristics and surface texture; and (6) integrated interpretation, including delineation of alteration domains, structural controls, and prioritization of exploration targets.

Lineament Orientation Analysis (Rose Diagrams)

Rose diagrams were constructed from the visually interpreted principal lineament orientations identified in the satellite imagery. Because the mapped trends are axial rather than directional, each measurement was treated in the 0–180° domain and expressed using the acute NE convention. For statistical treatment, axial data were transformed by angle doubling (2θ), allowing calculation of the mean orientation, mean resultant length ($\bar{R}$), and axial circular standard deviation. The mean trend was then back-transformed to the original NE–SW strike domain by halving the doubled-angle mean. In the plotted diagram, individual measurements are shown as mirrored axial rays, whereas the mean axial direction is highlighted in cyan. The Rayleigh test statistic is included as an indicative measure of clustering, but is interpreted cautiously owing to the small sample size. In IOCG-style settings, rose-diagram analysis is of additional practical relevance because many surface lineaments, including erosional expressions, may preferentially follow tectonically pre-weakened structures. Their orientation pattern can therefore assist in contextualizing the structural grain of the prospect and in supporting interpretation of possible mineralization controls, including zones that may also attract artisanal exploitation. As a reproducibility check, the interpreted lineaments were additionally digitized as vector features in QGIS using GeoTrace; strike data were exported to CSV, and the rose diagram was subsequently computed in Python.

Results and Discussion

The Results and Discussion section is structured as a staged demonstration of this workflow. Target 1 is treated as the benchmark case because it allows the full progression from very-high-resolution image discrimination to structurally contextualized geological interpretation to be shown in detail, whereas Target 2 is presented subsequently as a second application illustrating transferability under related but distinct surface-expression conditions.

Target 1: RGB-to-HSV transformation

Very-high-resolution Airbus Pléiades imagery was used for site-scale interpretation. With a native spatial resolution of approximately 0.7 m and standard visual products commonly resampled to 0.5 m, Pléiades imagery resolves local tonal and surface-textural variability that is not resolvable in Sentinel-2 true-color imagery at 10 m spatial resolution (Figure 4).

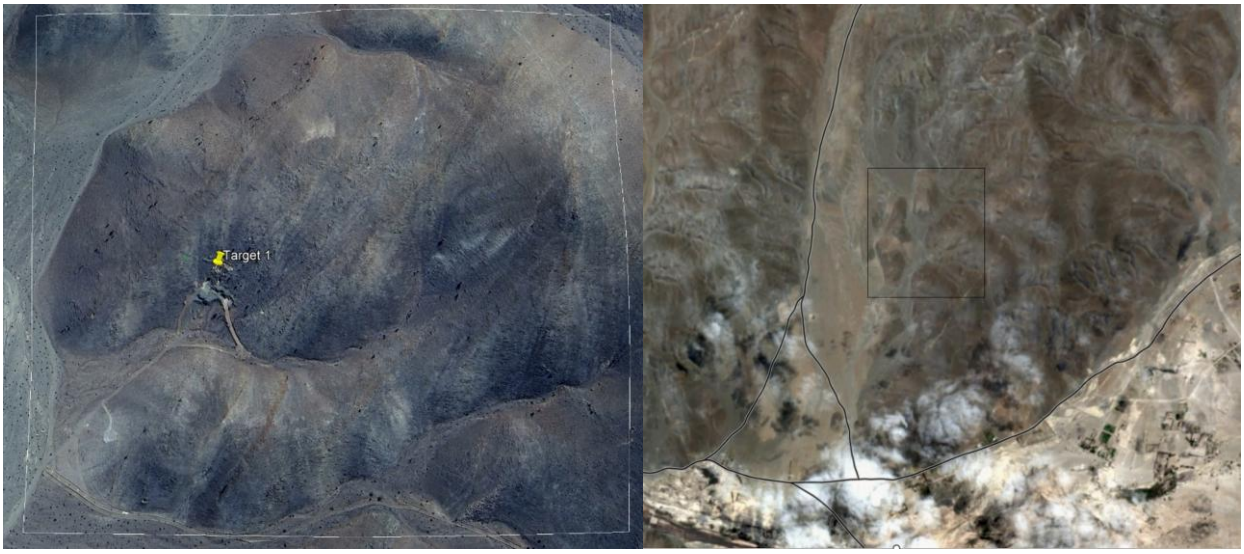

Figure 4. Left: Airbus Pléiades imagery of Target 1 (WGS84: −28.126503°, −70.863286°) in the Carrizal Alto Este region, acquired on 22 August 2023 and visualized in Google Earth Pro in 2026, showing the delineated analysis window (white polygon; approximately 0.3 km²) used for pixel-based evaluation and object-based image analysis (OBIA). The very-high-resolution imagery captures local tonal and surface-textural variability provisionally interpreted as oxidation-related domains and structurally influenced erosional features. Left-panel source: Google Earth/Google Earth Pro; Pléiades © CNES/Airbus DS; author overlay. Right: Sentinel-2 true-color composite (Bands 4–3–2) showing the same area at lower spatial resolution, where the fine-scale tonal and textural variability visible in the Pléiades imagery is not resolved. Right-panel source**:** Copernicus Sentinel-2 true-color composite, processed by the authors.

This comparison justifies retaining spatial resolution as a methodological issue in the workflow, because the two panels demonstrate that platform resolution directly controls the scale at which alteration-related surface features and structural context can be interpreted. As the interpretive challenge at Target 1 lies in subtle, spatially discontinuous, and structurally

partitioned surface expression, the analysis must therefore proceed from the dataset that best resolves local textural and geomorphological variability. For this reason, the subsequent interpretation is based principally on Airbus Pléiades imagery, while Sentinel-2 is used only as a secondary comparative reference.

With this scale-dependent image basis established, the next interpretive step is to examine whether the visible surface organization follows a coherent structural grain. The high spatial resolution of Airbus Pléiades imagery facilitates the identification of fault systems that would otherwise be difficult to detect, even at the local scale (Figure 5).

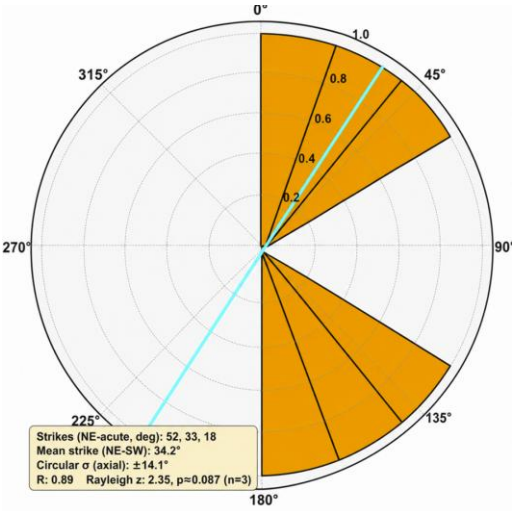

Figure 5. Rose diagram under the NE–SW convention, with acute strike directions oriented toward the northeast. The measured acute NE strikes are 52°, 33°, and 18°, yielding a descriptive mean NE–SW strike of 34.2° with an axial circular standard deviation of ±14.1°. The cyan ray marks the mean NE–SW orientation of approximately 34° and its axial equivalent. The diagram is intended as a descriptive summary of the observed fracture-orientation pattern rather than as a formal statistical test.

Establishing a coherent structural grain at Target 1 is important because the prospect does not display the broad, visually intuitive oxidation cap commonly associated with classical gossan systems. To clarify this contrast, a comparative analysis was conducted using a well-expressed gossan system developed over a mid-Miocene intrusive complex in the Precordillera east of Santiago. This reference example (Figure 6) shows a broad, laterally continuous, high-reflectance reddish-brown surface expression, with strong geomorphological relief and coherent radial to sub-radial drainage organization around the intrusive center. These features are consistent with a well-developed oxidized surface cap above sulfide-bearing mineralization and provide a useful reference case against which the more subtle surface expression at Target 1 can be compared.

The rose diagram derived from the same reference area (Figure 7) indicates that the fracture-strike population is not randomly distributed, but broadly organized around a principal

deformation zone and associated Riedel-type orientations. This supports the interpretation that the drainage and erosional architecture of the reference system is structurally guided, while remaining superimposed on a laterally coherent oxidized surface expression.

In contrast, Target 1 (Figure 4) displays a more spatially restricted and texturally heterogeneous surface expression, in which tonal contrasts are subdued and closely coupled to structurally controlled erosional features. This contrast illustrates that, unlike well-expressed porphyry-related or gossan-style systems, IOCG-style alteration may not produce regionally continuous or visually diagnostic oxidation caps. Instead, interpretation must rely on subtle textural, structural, and geomorphological proxies resolved at high spatial resolution.

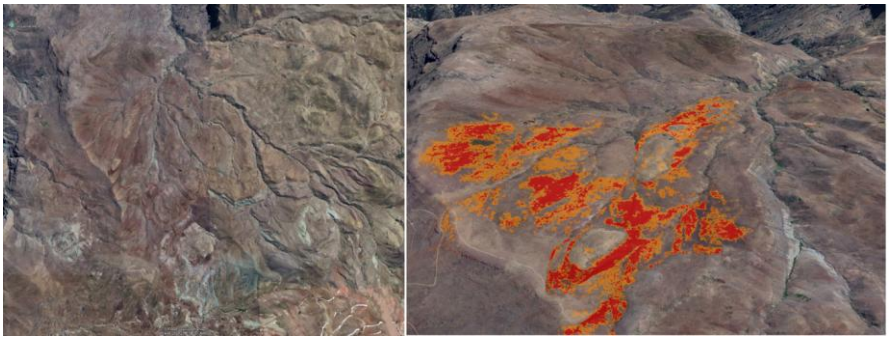

Figure 6. Comparative satellite imagery of a mid-Miocene intrusive system in the Precordillera east of Santiago, used as a reference example of a laterally extensive oxidation cap. Left: Airbus Pléiades image acquired on 19 March 2024 (image midpoint, WGS84: −33.415697°, −70.324756°; UTM Zone 19S), showing a broad, high-reflectance gossan-like surface expression with reddish-brown tonal domains and radial to sub-radial drainage organization. Right: false-color derivative map of the same area, using a red–orange–gray hierarchy to represent strong, moderate, and lower-intensity inferred Fe-oxide expression. Base imagery: Google Earth/Google Earth Pro; Pléiades imagery © CNES/Airbus DS where indicated. False-color processing, overlays, and annotations by the authors.

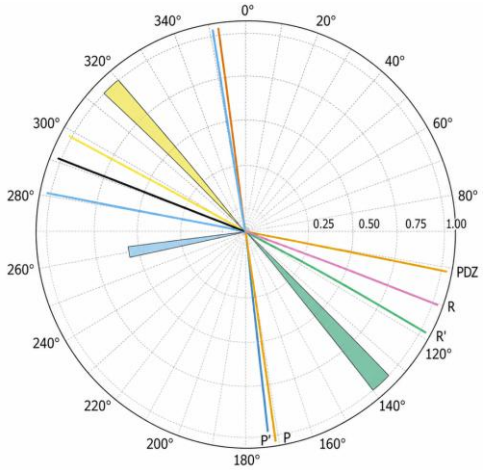

Figure 7. Rose diagram of weighted fracture-strike orientations interpreted from the Airbus Pléiades image of the comparative Precordillera gossan system. A Riedel-style overlay is shown for reference, including the principal deformation zone (PDZ; 101.0°/281.0°), synthetic R orientation (118.0°/298.0°), antithetic R′ orientation (173.0°/353.0°), P-shear reference (111.0°/291.0°), and interpreted P′ orientation (171.0°/351.0°).

The contrast with the Precordillera reference case underscores why Target 1 cannot be interpreted reliably through unaided visual inspection alone. In the absence of a laterally coherent gossan blanket, geological reasoning must instead proceed through an explicit interpretive framework that links subtle color variation, surface texture, and geomorphological position to provisional surface-expression classes. This role is fulfilled by the HSV-based heuristic proxy framework introduced below.

Interpretation of the Pléiades scene was guided by an HSV-based framework in which hue (H), saturation (S), and value/brightness (V) were evaluated together with visual texture and spatial or morphometric context. The classification scheme is intentionally conservative and image-based; the resulting classes are therefore used as interpretive surface proxies only and do not represent direct mineral-phase mapping or mineralogically verified classification.

The HSV criteria summarized in Table S1 provided the general interpretive basis for distinguishing major surface-expression domains within the Pléiades imagery. This table establishes the conservative reasoning framework at the level of image attributes, visual texture, and geomorphological context. To make these domains operationally visible in the enhanced image product, the HSV framework was then translated into a false-color classification scheme (Table S2), in which enhanced red–orange–yellow, magenta–pink–violet, blue–cyan, dark blue–gray, and localized green signatures were linked to provisional surface classes. These classes were interpreted respectively as Fe^{3+}-oxide-rich domains, probable hydrothermal halo expressions, clay-rich or weakly altered zones, comparatively unaltered host-rock surfaces, and possible moisture-related responses. The resulting map (Figure 8) should therefore be read as the spatial application of this two-stage workflow rather than as a direct mineral-phase classification. Whereas Table S2 defines the meaning of the principal color classes in terms of represented surface features and provisional geological significance, Figure 8 translates those classes into their spatial distribution across the Target 1 area. In this way, the false-color rendering supports recognition of spatial relationships among oxidation, alteration, slope processes, and structurally guided surface organization, while remaining a provisional surface-expression interpretation that requires field or analytical validation.

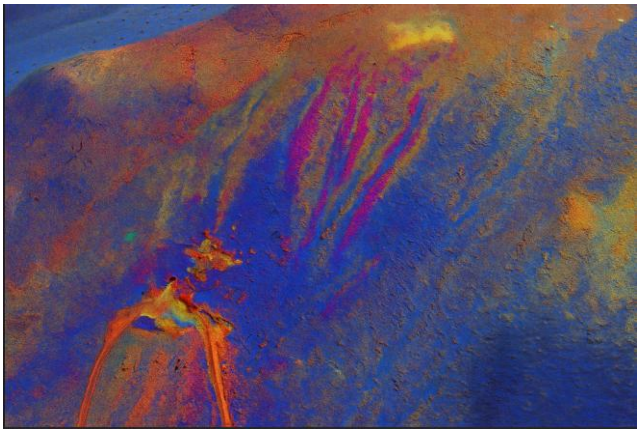

Figure 8. Enhanced false-color map of the Target 1 analysis area derived from Airbus Pléiades imagery, showing the spatial expression of the interpretive classes defined in Tables S1 and S2. The composite highlights oxidation-related domains, alteration-associated linear “finger-like” features, weakly altered host-rock surfaces, and localized moisture-related patches within a structurally influenced erosional setting. Source imagery: Google Earth / Google Earth Pro; Pléiades imagery © CNES/Airbus DS. False-color processing, classification, and annotations by the authors.

Target 1: From spectral proxy to actionable geological interpretation

Up to this point, the analysis of Target 1 has focused on establishing a reproducible framework for recognizing and spatially organizing surface-expression domains in the Pléiades scene. The next step is interpretive rather than purely classificatory: to examine how these mapped color and texture patterns can be reorganized into a geologically coherent model of oxidation zoning, structural control, and target significance. This transition is made explicit in Figure 8, which presents a two-stage representation of the near surroundings of the artisanal workings (approximately 0.6 ha).

The first stage focuses on the extraction and classification of iron oxide–related surface expressions from HSV-transformed RGB imagery, while the second stage integrates these spectral domains with morphostructural context to derive an interpretive geological model. This progression highlights the capacity of a low-cost, image-based workflow to support spatially explicit geological reasoning under data-limited conditions.

In Figure 9 (left), the distribution of iron oxide proxies is represented in simplified form, distinguishing between hematite-dominant, goethite/limonite-dominant, and jarosite-bearing surface expressions. These classes are derived from hue–saturation relationships and reflect relative differences in oxidation state and alteration intensity. The resulting map provides a descriptive but spatially coherent representation of surface mineralogical variability.

Figure 9 (right) illustrates the interpretive integration of these spectral patterns. The classified domains are combined with geomorphological observations and structural cues to produce a conceptual model of the mineralized system. In this representation, a continuous iron-oxide halo is delineated, within which a preferentially oriented corridor of enhanced mineralization is

inferred. Variations in iron oxide composition are interpreted as reflecting oxidation gradients and fluid pathways, consistent with structurally controlled supergene enrichment processes. The comparison between the left and right panels demonstrates the transition from spectral proxy mapping to decision-oriented geological interpretation. Whereas the left panel captures the spatial distribution of iron oxide–related surface signatures, the right panel translates these patterns into a coherent exploration model that supports target delineation and prioritization. This interpretive step does not introduce new data, but rather reorganizes existing image-derived information into a form that is directly applicable to early-stage exploration.
Overall, this example underscores the interpretive value of very-high-resolution RGB imagery when combined with systematic color-space transformation and contextual geological reasoning. Even in the absence of hyperspectral data or field calibration, such workflows can provide a defensible first-order approximation of alteration patterns and structurally controlled mineralization, thereby contributing to efficient reconnaissance and target generation in low-data environments.

Figure 9. Left: simplified classification of iron-oxide surface expressions derived from HSV-transformed RGB imagery, highlighting the relative distributions of hematite, goethite/limonite, and jarosite within the target area. Right: interpretive overlay illustrating how these spectral proxies can be translated into a structurally coherent mineralization model, including delineation of the iron-oxide halo and inferred mineralized corridor. Dark patches in the right panel represent surficial excavation sites related to artisanal workings. The left panel represents the analytical classification, whereas the right panel demonstrates how the same image-derived information can be reorganized for target prioritization in a low-data exploration context. Source imagery: Google Earth / Google Earth Pro; Pléiades imagery © CNES/Airbus DS. HSV classification, interpretive overlay, and annotations by the authors.

The interpretive utility of this framework is further illustrated by applying it beyond the immediate artisanal-workings area to a second nearby surface expression within the broader Target 1 domain. This additional zone is important because it shows that the workflow does not only rationalize the already disturbed focal area, but also assists in recognizing adjacent prospective ground that merits follow-up attention. Approximately 50 m east of the midpoint of Target 1 (Figure 10), an additional iron-oxide surface expression covering about 8.6 ha was

identified. The area is interpreted as a structurally controlled hydrothermal alteration zone within a known IOCG setting, characterized by intense supergene iron-oxide staining expressed as an inferred hematite–goethite–jarosite (red–orange–yellow) sequence, and is considered prospective for future exploration and possible exploitation.

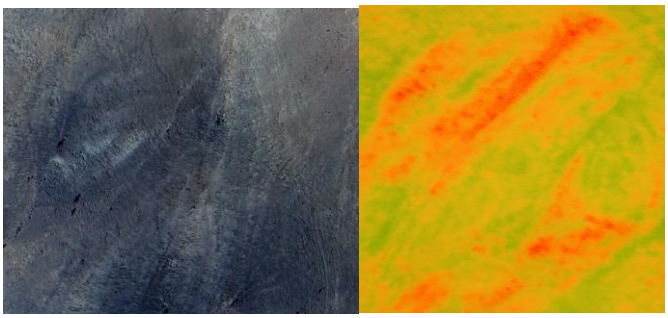

Figure 10. Additional structurally controlled iron-oxide alteration zone located approximately 50 m east of the midpoint of Target 1. The left panel shows the original high-resolution image, whereas the right panel presents an interpretive rendering of the same area, in which the red–orange–yellow progression denotes an inferred hematite–goethite/limonite–jarosite surface-expression sequence. The zone is characterized by intense supergene iron-oxide staining within a known IOCG setting and is interpreted as a prospective target for follow-up exploration. Source imagery: Google Earth / Google Earth Pro; Pléiades imagery © CNES/Airbus DS. Interpretive rendering by the authors.

Target 2: RGB-to-HSV transformation

Having developed the full interpretive sequence for Target 1 as the benchmark case, the analysis now turns to Target 2 in order to evaluate whether the same low-cost image-based logic remains informative in a second IOCG-style setting with a different balance of preserved Fe-oxide cap, erosional modification, and artisanal disturbance.

Consistent with the approach applied to Target 1, site-scale interpretation of Target 2 was based on very-high-resolution Airbus Pléiades imagery, whose finer spatial detail allows recognition of local tonal and surface-textural variability not resolved in Sentinel-2 true-color imagery (Figure 11). The visual contrast between the two datasets is especially evident in the sharper definition of narrow lineaments, tonal boundaries, and local erosional textures in the Pléiades image. Despite its lower spatial resolution, Sentinel-2 imagery provides a useful supplementary perspective in this case because its later acquisition date allows recognition of surface changes that postdate the 2023 Airbus Pléiades scene. Whereas the earlier Pléiades image records only limited small-scale disturbance over much of the Target 2 area, the 2025/2026 Sentinel-2 image suggests that artisanal mining-related ground disturbance had subsequently expanded across broader sectors of the prospect. Sentinel-2 is therefore used here not for fine-scale surficial interpretation, but for multi-temporal contextualization of later surface modification once the spatial footprint of disturbance becomes sufficiently large to be expressed at 10 m resolution.

Figure 11. Two-panel view of Target 2 (centered at 28.894861° S, 71.089119° W; WGS84), combining high-resolution image interpretation with later temporal comparison. Left: Airbus Pléiades imagery acquired on 17 September 2023 and displayed in Google Earth Pro in 2026, providing site-scale resolution of tonal variability, erosional textures, and narrow structural lineaments. Right: Sentinel-2 imagery from 2025/2026, used primarily as a later temporal reference; although its spatial resolution is insufficient for fine surficial detail, it records broader ground-pattern changes that postdate the 2023 Pléiades image and are consistent with expanded artisanal surface disturbance. Panel sources: left, Google Earth / Google Earth Pro; Pléiades imagery © CNES/Airbus DS; overlays and annotations by the authors. Right, Copernicus Sentinel-2 data, processed by the authors.

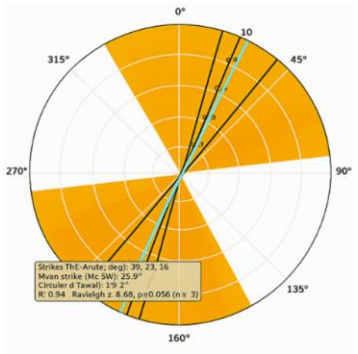

Figure 12. Rose diagram of the principal interpreted lineaments at Target 2, plotted as axial orientations with mirrored rays and a cyan mean trend, summarizing the dominant NE–SW structural alignment.

To move beyond direct visual inspection, the RGB image was transformed into HSV color space, separating hue, saturation, and value into analytically distinct components. This approach allowed subtle surface variability to be examined and supported the identification of domains potentially related to oxidation patterns, alteration, and structural control (Figure 13). The mapped pattern indicates that Target 2 is characterized by a heterogeneous alteration mosaic rather than a single, laterally uniform surface expression. Fe-oxide-rich domains, probable hydrothermal halo expressions, weakly altered clay-rich surfaces, and comparatively less altered host-rock domains are spatially interleaved across the target area. This arrangement supports

the interpretation of Target 2 as a structurally and geomorphologically complex surface system in which oxidation-related and alteration-related responses are discontinuously exposed.

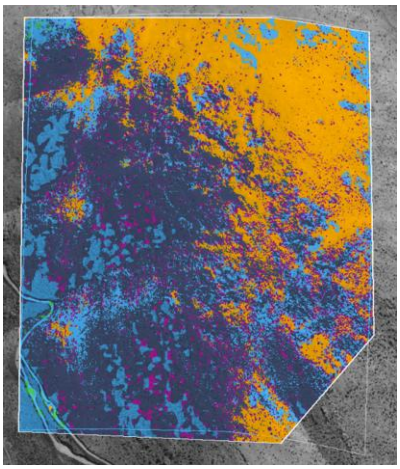

Figure 13. False-color interpretation map for Target 2, showing surface domains classified within the outlined analysis window from RGB–HSV-based visual analysis. The color scheme is interpretive and emphasizes relative surface-expression contrasts rather than directly mapped mineral phases. Red–orange–yellow domains indicate Fe^{3+}-oxide-rich or gossan-like surface expressions; magenta–pink–violet zones denote probable hydrothermal halo domains; blue–cyan areas indicate clay-rich or weakly altered surfaces; and dark blue–gray domains represent comparatively unaltered or less visibly altered host-rock surfaces. Isolated green patches, where present, are interpreted cautiously as possible moisture-related surface responses rather than primary alteration signals. Source imagery: Google Earth / Google Earth Pro; Pléiades imagery © CNES/Airbus DS. RGB–HSV processing, classification, and annotations by the authors.

A simplified Fe-oxide–dominant proxy map was derived by isolating red–orange–yellow HSV domains, representing zones of elevated iron-oxidation intensity (Figure 14, left). The asymmetric distribution of Fe^{3+}-oxide signatures, with a well-developed gossan-like expression in the eastern sector and a markedly subdued response in the western sector, is interpreted to reflect partial erosional removal of the iron-oxide cap. When structural and topographic interpretation is added, the western area, currently affected by localized artisanal excavation, coincides with zones of reduced Fe-oxide expression and lower elevation, suggesting that the oxidized cap may have been stripped and that underlying alteration or possible sub-cap mineralization is locally exposed (Figure 14, right). This spatial relationship supports the interpretation that artisanal activity preferentially targets exposed or near-surface sub-cap material rather than the preserved Fe-oxide cap itself.

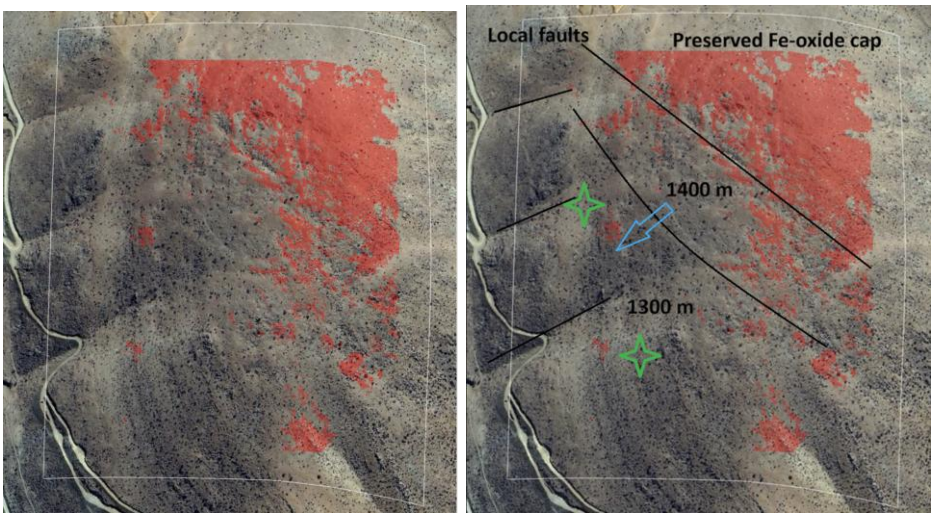

Figure 14. Two-panel interpretation of Target 2 based on HSV-derived Fe-oxide proxy mapping. Left: simplified Fe-oxide–dominant proxy map derived from HSV-based classification of the Target 2 area. Red zones represent areas of elevated Fe^{3+}-oxide expression, shown here as a hematite–goethite–jarosite-like composite surface response, and highlight the spatial footprint of oxidized surface material within the outlined analysis window. Right: Fe-oxide proxy overlay integrated with structural and topographic interpretation. The preserved Fe-oxide cap is concentrated mainly at higher elevation near the ~1400 m level, whereas lower areas near the ~1300 m level show reduced Fe^{3+}-oxide expression interpreted as erosional removal of the iron-oxide cap. The blue arrow indicates the inferred local erosion gradient. Green four-point stars mark visible artisanal excavation sites. Thin black lineaments indicate interpreted local faults that appear to influence oxidation patterns and excavation activity. Source imagery: Google Earth / Google Earth Pro; Pléiades imagery © CNES/Airbus DS. HSV processing, proxy mapping, interpretive overlay, and annotations by the authors.

Conclusion

This study illustrates a multi-stage progression from remotely sensed imagery to geological interpretation under minimal-data conditions. For both Target 1 and Target 2, the workflow proceeds from the Google Earth base image, which establishes geomorphological context, through pixel-wise HSV-based classification highlighting spectral-proxy domains, to simplified Fe-oxide–dominant overlays that emphasize zones of elevated Fe^{3+}-oxide expression. This progression demonstrates how spectral and tonal surface information can be translated into spatially coherent geological interpretation, supporting delineation of oxidized mineralization, structurally controlled alteration patterns, and lineament-guided exploration targets. While the results remain interpretive and should be validated by field and analytical follow-up, the approach is of practical significance for small-scale mining and early-stage exploration settings, where financial and technical constraints commonly preclude more sophisticated remote-sensing workflows. In such contexts, the method provides a low-cost and operationally relevant means of identifying prospective surface expressions and prioritizing areas for subsequent investigation.

Author contributions

Conceptualization, H.K.; methodology, H.K.; investigation, H.K.; formal analysis, H.K.; visualization, H.K. and K.T.; software and computational workflow support, K.T.; geological interpretation, H.K.; surveying-related technical input, K.T.; writing—original draft preparation, H.K.; writing—review and editing, H.K. and K.T. All authors have read and approved the final version of the manuscript submitted to EarthArXiv as a preprint.

Use of geoinformatics and AI tools

The authors acknowledge the use of geoinformatics software and AI-assisted language and technical-editing tools during manuscript preparation. AI-assisted tools were used for language refinement, editorial structuring, figure-caption drafting support, and consistency checks. All geological interpretations, methodological decisions, source selection, verification of cited information, and final responsibility for the manuscript remain solely with the authors.

Conflicts of interest

The authors declare no conflicts of interest.

Data availability

The derived data supporting the findings of this study, including additional computational details and intermediate analytical outputs, are contained within the article and the Supplementary Information. Third-party satellite imagery used for visual interpretation is available from the respective data providers under their applicable access and licensing conditions and is not redistributed separately.

License and third-party material

References

Advanced Mining Technology Center. (2021). *Transformación digital en la mediana y pequeña minería chilena: Caracterización de la mediana y pequeña minería, nivel de conocimiento en transformación digital y propuesta de matriz de madurez tecnológica*. Sociedad Nacional de Minería & Cisco Systems Chile. https://www.sonami.cl/v2/wp-content/uploads/2022/06/Informe-Estudio-Transformacion-Digital-en-MM.pdf

Arabameri, A., Tiefenbacher, J. P., Blaschke, T., Pradhan, B., & Bui, D. T. (2020). Morphometric analysis for soil erosion susceptibility mapping using novel GIS-based ensemble model. *Remote Sensing, 12*(5), Article 874. https://doi.org/10.3390/rs12050874

Badr, M. M., El Mezayen, A. M., El Azab, A., & Elyaseer, M. H. (2026). Integrated multispectral remote sensing and field investigations for delineating ophiolitic complexes of Wadi Ghadir, southeastern Desert, Egypt. *Scientific Reports, 16*, 798. https://doi.org/10.1038/s41598-025-32272-8

Blaschke, T. (2010). Object based image analysis for remote sensing. *ISPRS Journal of Photogrammetry and Remote Sensing, 65*(1), 2–16. https://doi.org/10.1016/j.isprsjprs.2009.06.004

Blein, O., Harlaux, M., Corriveau, L., Niiranen, T., Lynch, E. P., Lisitsin, V., Ehrig, K., Montreuil, J.-F., & Gourcerol, B. (2025). Geochemical footprints of IOA and IOCG deposits in northern Norrbotten, Sweden, and Cloncurry District, Australia. *Journal of Geochemical Exploration, 277*, 107820. https://doi.org/10.1016/j.gexplo.2025.107820

Chernov, V., Alander, J., & Bochko, V. (2015). Integer-based accurate conversion between RGB and HSV color spaces. *Computers & Electrical Engineering, 46*, 328–337. https://doi.org/10.1016/j.compeleceng.2015.08.005

Copernicus Sentinel-2 (processed by ESA). (2021). *MSI Level-1C TOA reflectance product: Collection 1* [Data set]. European Space Agency. https://doi.org/10.5270/S2_-742ikth

Deckart, K., Godoy, E., Bertens, A., Jerez, D., & Saeed, A. (2010). Barren Miocene granitoids in the Central Andean metallogenic belt, Chile: Geochemistry and Nd-Hf and U-Pb isotope systematics. *Andean Geology, 37*(1), 1–31. https://doi.org/10.4067/S0718-71062010000100001

El-Wardany, R., Jiao, J., Zoheir, B., Khedr, L., Kumral, M., Liu, L., Abu El-Leil, I., Orabi, A., Abd El-Salam, L., & Abdelnasser, A. (2025). Remote sensing-based machine learning techniques for mapping gold-mineralized alteration zones in the Fatira Mine area, Egypt. *Acta Geologica Sinica: English Edition, 99*, 1196–1223. https://doi.org/10.1111/1755-6724.15333

Fotze, Q. M. A., Lordon, A. E. D., Penaye, J., Sep, J. P., & Fru, M. I. N. (2019). Mapping hydrothermal alteration targets from Landsat 8 OLI/TIRS and magnetic data using digital image processing techniques in Garoua, North Cameroon. *Journal of Geosciences and Geomatics, 7*(1), 28–41. https://doi.org/10.12691/jgg-7-1-4

González, G., Cembrano, J., Carrizo, D., Macci, A., & Schneider, H. (2003). The link between forearc tectonics and Pliocene–Quaternary deformation of the Coastal Cordillera, northern Chile. *Journal of South American Earth Sciences, 16*(5), 321–342. https://doi.org/10.1016/S0895-9811(03)00100-7

Google. (2026). *Google Earth Pro* [Satellite images of Target 1, Coastal Cordillera, Atacama Region, Chile, and Target 2, Precordillera east of Santiago, central Chile; Airbus Pléiades imagery dated January 28, 2023, and August 22, 2023]. https://earth.google.com/

Hajaj, S., El Harti, A., Pour, A. B., Jellouli, A., Adiri, Z., & Hashim, M. (2024). A review on hyperspectral imagery application for lithological mapping and mineral prospecting: Machine learning techniques and future prospects. *Remote Sensing Applications: Society and Environment, 35*, 101218. https://doi.org/10.1016/j.rsase.2024.101218

Hu, Q., Wu, W., Xia, T., Yu, Q., Yang, P., Li, Z., & Song, Q. (2013). Exploring the use of Google Earth imagery and object-based methods in land use/cover mapping. *Remote Sensing, 5*(11), 6026–6042. https://doi.org/10.3390/rs5116026

Japan International Cooperation Agency. (2005). Estudio de la influencia de las actividades mineras de mercurio en la comarca de Almadén (Report No. 11816691). https://openjicareport.jica.go.jp/pdf/11816691_03.pdf

Kurata, K., & Yamaguchi, Y. (2019). Integration and Visualization of Mineralogical and Topographical Information Derived from ASTER and DEM Data. *Remote Sensing, 11*(2), 162. https://doi.org/10.3390/rs11020162

Lawal, M. A., Oshomoji, A. O., Akinlalu, A. A., Adebayo, A. S., Aladejana, O. O., & Babalola, A. O. (2022). A simplified GIS and Google Earth–based approach for lineaments and terrain attributes mapping in a basement complex terrain. *Scientific Reports, 12*, 15801. https://doi.org/10.1038/s41598-022-20057-2

Mahanta, P., & Maiti, S. (2021). Regional scale alteration mineral mapping using ASTER imagery in sparsely vegetated terrain: A case study from the eastern part of the South Purulia Shear Zone, India. *International Advanced Research Journal in Science, Engineering and Technology, 8*(8), 597–607. https://doi.org/10.17148/IARJSET.2021.8899

Mohamed, A., Emam, A., & Zoheir, B. (2023). SAM-HIT: A simulated annealing multispectral to hyperspectral imagery data transformation. *Remote Sensing, 15*(4), 1154. https://doi.org/10.3390/rs15041154

Orynbassarova, E., Ahmadi, H., Beiranvand Pour, A., Yerzhankyzy, A., Zakariya, M., & Omirzhanova, Z. (2025). PRISMA hyperspectral satellite imagery for mapping alteration minerals and zones in the Aktogay porphyry copper deposit, Kazakhstan: Implications for new discoveries. *Geocarto International, 40*(1), Article 2591763. https://doi.org/10.1080/10106049.2025.2591763

Pour, A. B., & Hashim, M. (2012). The application of ASTER remote sensing data to porphyry copper and epithermal gold deposits. *Ore Geology Reviews, 44*, 1–9. https://doi.org/10.1016/j.oregeorev.2011.09.009

Scheuber, E., & Gonzalez, G. (1999). Tectonics of the Jurassic–Early Cretaceous magmatic arc of the north Chilean Coastal Cordillera (22°–26°S): A story of crustal deformation along a convergent plate boundary. *Tectonics, 18*(5), 895–910. https://doi.org/10.1029/1999TC900024

Servicio Nacional de Geología y Minería. (2003). *Mapa geológico de Chile: Versión digital* (Publicación Geológica Digital No. 4, CD-ROM, versión 1.0; escala 1:1.000.000) [Digital geological map].

Smith, A. R. (1978). Color gamut transform pairs. *ACM SIGGRAPH Computer Graphics***,** 12(3), 12–19. https://doi.org/10.1145/800248.807361

Upadhyay, R. K. (2025). Exploration of mineral resources. In R. K. Upadhyay (Ed.), *Geology and mineral resources* (pp. 655–723). Springer. https://doi.org/10.1007/978-981-96-0598-9_10

van der Meer, F. D., van der Werff, H. M. A., van Ruitenbeek, F. J. A., Hecker, C. A., Bakker, W. H., Noomen, M., van der Meijde, M., Carranza, E. J. M., de Smeth, J. B., & Woldai, T. (2012). Multi- and hyperspectral geologic remote sensing: A review. *International Journal of Applied Earth Observation and Geoinformation, 14*(1), 112–128. https://doi.org/10.1016/j.jag.2011.08.002

Supplementary Information

Regional geological-map legend and lithostratigraphic context

This section provides geological-map legends supporting Figures 1 and 2 and summarizes the lithostratigraphic units relevant to the Target 1 and Target 2 areas, as well as to the comparative example. The legends are included separately to preserve the readability of the main regional-setting figures while retaining the original geological context from SERNAGEOMIN (2003).

Figure S1. Enlarged geological-map legend for the lithostratigraphic units highlighted in Figure 1. Unit descriptions are translated from the original Spanish legend of SERNAGEOMIN (2003).

Jsg — Middle–Upper Jurassic (180–142 Ma)
Quartz monzodiorites, diorites, and biotite-, pyroxene- and hornblende-bearing granodiorites. In the Coastal Cordillera, Regions I–VI; in the Principal Cordillera, Regions X and XI: Panguipulli Pluton and eastern margin of the North Patagonian Batholith; in the Antarctic Peninsula.
Kibg — Lower Cretaceous, lower interval (144–124 Ma)
Pyroxene-, hornblende- and biotite-bearing monzodiorites and diorites, granodiorites, and tonalites. In the Coastal Cordillera, Regions II–IV, associated with the Atacama–El Romeral Fault System and Fe mineralization at Cerro Imán and Algarrobo.

Figure S2. Enlarged geological-map legend for the lithostratigraphic units highlighted in Figure 2. Unit descriptions are translated from the original Spanish legend of SERNAGEOMIN (2003).

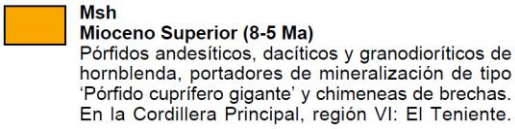

Msh — Upper Miocene (8–5 Ma)
Hornblende-bearing andesitic, dacitic and granodioritic porphyries, hosting 'giant porphyry copper'-type mineralization and breccia pipes. In the Principal Cordillera, Region VI: El Teniente.

Use of image-based interpretive surface proxies

Table S1 represents the rule-based framework used for heuristic surface-proxy mapping, in which combinations of HSV properties, visual texture, and spatial context are assigned to interpretive surface classes. These classes are used solely as image-based interpretive proxies and do not represent direct mineral-phase mapping or mineralogically verified classification.

Table S1. Heuristic RGB–HSV criteria for image-based surface-proxy classification.

HSV/visual criterion	Spatial or morphometric context	Interpretive surface class and rationale
Red–orange hue (H) range, with moderate to high saturation (S) and moderate value/brightness (V); locally reduced V may reflect shadowing	Spatially coherent patches or cap-like domains, commonly ridge-forming or erosion-resistant	Fe^{3+}-oxide-rich oxidized surfaces/ gossan-like domains; indicative of Hem–Gth oxidation and possible local supergene enrichment
Yellow–orange to brownish or subdued warm H, with moderate to low S and variable V	Transitional or diffuse halos surrounding stronger Fe-oxide domains	Hem–Jrs–Gth/Lim-type Fe^{3+} oxide–oxyhydroxide–sulfate surface expression; hydrated Fe-oxide alteration halos and/or peripheral weathering zones
Low S with strong V gradients and smooth slope textures	Slope-mantling or erosional surfaces, including colluvial or fine-grained accumulations	Clay-rich or weakly altered slope deposits; reflects fine-grained material with subdued spectral contrast
Low chromatic contrast with relatively stable V	Background surfaces outside mapped alteration domains or structurally continuous background areas	Weakly altered or comparatively unaltered host rock; represents minimally altered lithologies with limited oxidation signature
Localized green H with locally high S and elevated or variable V	Topographic depressions, drainage-related positions, or convergence zones	Moisture-related, non-mineralized surface response; interpreted as moisture or vegetation effects rather than mineralization

Mineral abbreviations: Hem = hematite; Jrs = jarosite; Gth = goethite; Lim = limonitic Fe-oxyhydroxide material used as a descriptive proxy term.

Table S2 presents a false-color interpretation framework for rendered Airbus Pléiades composites. It summarizes the relationship between enhanced color channels, inferred surface features, typical image appearance, and provisional geological interpretation. Red–orange–yellow tones are interpreted as Fe^{3+}-rich oxidized surface expressions, locally including gossan-like domains; magenta–pink–violet tones as ferruginous to 3d transition-metal oxide/oxyhydroxide-bearing alteration zones, locally associated with Ilt–Sme–Chl-type phyllosilicate/clay alteration; blue–cyan tones as clay-rich or weakly altered domains; dark blue–gray tones as shadowed or relatively unaltered background surfaces; and isolated greenish spots as minor moisture-retaining or micro-vegetated niches. These categories are heuristic remote-sensing classes derived from image expression and spatial context, and do not constitute field-verified mineralogical or lithological determinations.

Table S2. False-color interpretation framework for rendered Airbus Pléiades composites.

False-color tone/ channel	Inferred surface feature	Typical image appearance	Provisional geological interpretation
Red–orange–yellow	Fe^{3+} oxide/oxyhydroxide/ sulfate-rich surface expressions, represented by Hem–Jrs–Gth-type assemblages	Bright zones in mining workings and linear "finger-like" extensions	Ferruginous cap or gossan-like surface expression, consistent with supergene oxidation and possible local metal enrichment or scavenging by Fe oxides
Magenta–pink–violet	Ferruginous to first-row transition-metal oxide/ oxyhydroxide-bearing alteration zones with associated phyllosilicate/ clay alteration, provisionally represented by Ilt–Sme–Chl-type surface expressions	Lineaments extending along vein structures, and/or overprinting breccia zones	Hydrothermal halos or oxidized veinlet zones with residual 3d transition-metal oxide/ oxyhydroxide-bearing surface expressions
Blue–cyan	Clay-rich/weakly altered domains; local Ilt–Sme–Chl-type phyllosilicate/clay halos (IOCG-style), or alteration envelope of phyllic–argillic affinity (porphyry Cu)	Slopes adjacent to mineralized lobes or alteration margins	Partially altered host rock with Ilt ± Kln-type phyllosilicate/clay alteration; subdued Fe-oxide expression
Dark blue–gray	Shadowed or relatively unaltered background surfaces	Uniform low-reflectance background	Volcanic, intrusive, or metasedimentary host rocks with no strong image-scale alteration expression
Greenish spots (isolated)	Local surface moisture or micro-vegetated niches	Small patches or narrow linear features	Minor moisture retention along fractures or drainage micro-sites; not interpreted as a primary alteration or mineralization proxy

Mineral abbreviations: Hem = hematite; Jrs = jarosite; Gth = goethite; Lim = limonitic Fe-oxyhydroxide material used as a descriptive proxy term; Ilt = illite; Sme = smectite; Chl = chlorite; Kln = kaolinite. The symbol ± indicates a possible or subordinate contribution. All mineral associations are used as image-based proxy expressions and do not imply field-verified mineral identification.

Computational details of RGB-to-HSV transformation

This section provides the computational basis for the RGB-to-HSV transformation used in the image-interpretation workflow. It also notes relevant data limitations and interpretive constraints where these affect the use of HSV-derived surface proxies.

RGB-to-HSV transformation

For each pixel, the red, green, and blue digital numbers were first read from the raster image as R, G, and B. In standard 8-bit imagery, these values lie in the range 0 to 255. They were then normalized to the interval [0,1]:

$$r = \frac{R}{255}, g = \frac{G}{255}, b = \frac{B}{255}$$

The maximum and minimum normalized channel values, denoted here as C_{max} and C_{min}, were defined as:

$$C_{\max} = \max(r, g, b)$$
$$C_{\min} = \min(r, g, b)$$
$$\Delta = C_{\max} - C_{\min}$$

The HSV components were then computed as follows:

Value

The value component *V* represents brightness and is given by:

$V = C_{max}$

Saturation

The saturation component *S* is defined as:

$$S = \begin{cases} 0, & \text{if } C_{\max} = 0 \\ \dfrac{\Delta}{C_{\max}}, & \text{if } C_{\max} \neq 0 \end{cases}$$

Thus, S ranges from 0 for gray tones to 1 for fully saturated colors.

Hue

The hue component *H*, expressed in degrees on the interval [0^o, 360^o], was computed by piecewise definition:

$$H = \begin{cases} 0, & \text{if } \Delta = 0 \\ 60^\circ \times \left(\frac{g-b}{\Delta} \bmod 6\right), & \text{if } C_{\max} = r \\ 60^\circ \times \left(\frac{b-r}{\Delta} + 2\right), & \text{if } C_{\max} = g \\ 60^\circ \times \left(\frac{r-g}{\Delta} + 4\right), & \text{if } C_{\max} = b \end{cases}$$

When Δ = 0, the pixel is achromatic and hue is formally undefined; in practice, it was assigned a value of 0 for computational convenience. If required for software implementation, hue can also be normalized to the interval [0,1] by H_norm = H/360.

Climate

Climatic setting is an important interpretive consideration in the present study because both targets are located in the hyper-arid Atacama Desert, where exceptional atmospheric clarity, extremely low humidity, intense solar irradiance, and the near absence of vegetation strongly condition the optical appearance of the land surface. Under such conditions, exposed rock and dust-covered rock surfaces are observed with minimal vegetative masking and limited moisture-related spectral damping, such that surface dryness tends to enhance the visibility of lithological and alteration-related tonal differences. At the same time, however, the apparent VIS/NIR response recorded in image products remains sensitive to illumination geometry, terrain aspect, and bidirectional reflectance effects, particularly in rugged topography. As a result, variations in brightness, color saturation, and apparent hue may reflect not only intrinsic material properties, but also the interaction between solar angle, surface roughness, dust cover, and slope-dependent shadowing. For this reason, the hyper-arid climatic context is not merely descriptive background, but forms part of the remote-sensing framework required to interpret RGB/HSV-derived surface patterns cautiously and in their proper environmental setting.

Both Target 1 and Target 2 were imaged by Airbus in August and September 2023, a period in the Chilean Atacama Desert characterized by extremely low atmospheric humidity and exceptionally high incoming solar radiation under persistently cloud-free skies. Although absolute radiation levels are higher during the austral summer, late winter and early spring still provide intense surface illumination because cloud-free conditions commonly exceed 90–95% of the time. In this hyper-arid, vegetation-free environment, exposed rock and dust-covered surfaces are therefore observed under conditions of high atmospheric clarity and surface dryness, which enhance optical visibility while also increasing the influence of illumination geometry and terrain shadowing on apparent surface color and tonal expression.

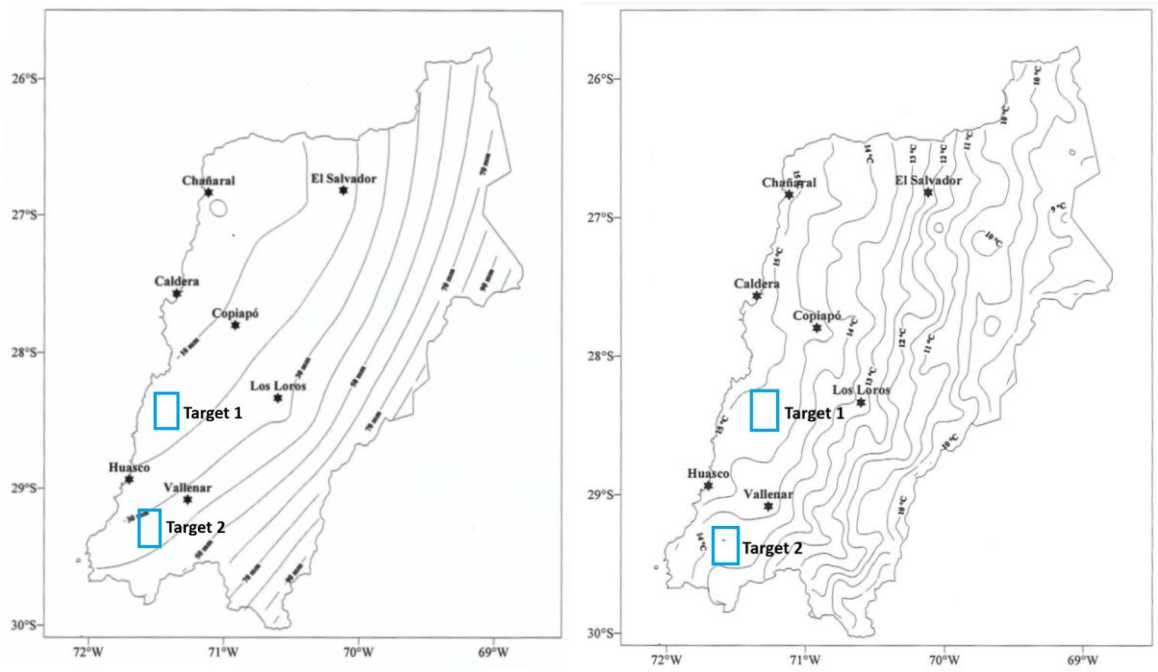

Figure S3. Left: The annual rainfall regime is characterized by very limited precipitation, with generally insignificant amounts that chiefly reflect the area's arid conditions, except in the higher parts of the region, where annual totals may reach up to 90 mm. Right: The longitudinal thermal pattern is modified by the region's two principal transverse valleys, those of the Copiapó and Huasco rivers. The steepest thermal gradient occurs in the transition from the valleys and transverse ranges to the Andes, where it reaches nearly 6 °C. Mean annual temperatures range from 9–11°C in the Andean sector of the region, from 11–14°C in the intermediate valleys, and from 14–15°C in the coastal zone. Translated from: Dirección Meteorológica de Chile, Departamento de Climatología y Meteorología. (2001), p. 11–12.

Previous Geological Assessment and Mining Activity

The Target 1 area forms part of the historic Carrizal Alto district, which gained international recognition during the nineteenth and twentieth centuries for cobalt production associated with copper and gold. Mining was conducted mainly through artisanal workings and small-scale crews, using manual methods and without systematic technical control.

Surface evidence of previous activity includes small open cuts, selective trenches excavated for Cu–Co oxides, partially collapsed shallow adits, and small waste dumps. These workings were concentrated where oxidation and metal enrichment were most strongly expressed, particularly along open fault corridors, hematitized zones containing thin veins, and violet to bluish halos associated with Fe–Mn alteration. Because efficient technologies for the separation of cobalt, nickel, and copper were not available at the time, a substantial proportion of the extracted material was not fully recovered or economically utilized.

Figure S4. Representative artisanal mining operation in the Carrizal Alto region. Image viewed in Google Earth Pro in 2026. Base imagery: Google Earth/Google Earth Pro; Pléiades imagery © CNES/Airbus DS where indicated.

Mineralization in the Target 2 area is hosted by brecciated rock carrying disseminated copper and gold. Previous exploration work in the district was reported by Guerrero (2016) in a technical study prepared for ENAMI. The geological characteristics described therein are consistent with the current understanding of IOCG-type deposit formation, as reviewed by Skirrow (2022). Within IOCG systems of the Coastal Cordillera of northern Chile, average copper grades commonly range from about 0.4–1.5% Cu, depending on the specific deposit and the mining method applied. Gold grades are typically lower, commonly averaging 0.1–0.3 g/t. In this context, the Target 2 occurrence is consistent with a breccia-hosted IOCG-style system of modest but regionally characteristic grade. Mining activity in the surrounding area includes small- to medium-scale operations such as Minas Félix and Rosita, Mina La Cuesta, and Mina Improvisada. In addition, several artisanal excavations appear to lack clear registration status and may be informal.

Figure S5. Left: Medium-scale mining operation at Félix. Right: unnamed artisanal excavation. Image viewed in Google Earth Pro (2026). Base imagery: Google Earth/Google Earth Pro; Pléiades imagery © CNES/Airbus DS where indicated.

Data limitations and interpretive constraints

The principal data limitations relate to the spatial resolution of the imagery and to topographic illumination effects. Although both target areas were imaged under cloud-free morning conditions, terrain roughness generated localized shadowing, particularly on west-facing slopes. This may attenuate the visible surface expression and alter the apparent RGB/HSV response, such that observed color contrasts do not always correspond exactly to intrinsic surface material properties. The image pair shown below, based on Maxar imagery widely used in Google Earth in recent years, illustrates illumination-induced interpretive uncertainty by showing how apparent surface color, tonal contrast, and landform expression may vary between morning and near-midday illumination under fall–winter conditions in the Atacama Desert.

Figure S6. Left: Maxar Technologies image acquired on 13 November 2014, showing late-spring near-midday illumination. Right: Maxar Technologies image acquired on 18 May 2009, showing late-fall morning illumination. The comparison demonstrates how illumination geometry can influence apparent surface color, tonal contrast, and geomorphic expression, thereby affecting geological interpretation. Both images were acquired in the Morado Sureste mining district, north and east of the Félix mine. Source imagery: Google Earth/Google Earth Pro; Maxar Technologies imagery © Maxar Technologies where indicated. Figure assembly and interpretation by the authors.

References cited in the Supplementary Information

Dirección Meteorológica de Chile, Departamento de Climatología y Meteorología. (2001). *Climatología regional*. Ministerio del Medio Ambiente. https://planesynormas.mma.gob.cl/archivos/2019/proyectos/Climatologia_Regional.pdf

Guerrero, N. (2016). *Geología del Distrito Minero El Morado Sureste* [Geology of the El Morado Sureste Mining District]. Empresa Nacional de Minería. https://www.scribd.com/document/442319662/INFORME-MORADO-SURESTE

Skirrow, R. G. (2022). Iron oxide copper-gold (IOCG) deposits—A review (part 1): Settings, mineralogy, ore geochemistry and classification. *Ore Geology Reviews, 140*, Article 104569. https://doi.org/10.1016/j.oregeorev.2021.104569